NANO LETTERS

pubs.acs.org/NanoLett Letter

Mechanical Anisotropy in Two-Dimensional Selenium Atomic Layers

Jing-Kai Qin,[∞] Chao Sui,[∞] Zhao Qin, Jianyang Wu, Hua Guo, Liang Zhen, Cheng-Yan Xu, Yang Chai, Chao Wang,* Xiaodong He,* Peide D. Ye,* and Jun Lou*

Cite This: https://doi.org/10.1021/acs.nanolett.1c02294 Read Online

ACCESS | Metrics & More | Article Recommendations | Supporting Information

ABSTRACT: Two-dimensional (2D) trigonal selenium (*t*-Se) has become a new member in 2D semiconducting nanomaterial families. It is composed of well-aligned one-dimensional Se atomic chains bonded via van der Waals (vdW) interaction. The contribution of this unique anisotropic nanostructure to its mechanical properties has not been explored. Here, for the first time, we combine experimental and theoretical analyses to study the anisotropic mechanical properties of individual 2D *t*-Se nanosheets. It was found that its fracture strength and Young's modulus parallel to the atomic chain direction are much higher than along the transverse direction, which was attributed to the weak vdW interaction between Se atomic chains as compared to the covalent bonding within individual chains. Additionally, two distinctive fracture modes along two orthogonal loading directions were identified. This work provides important insights into the understanding of anisotropic mechanical behaviors of 2D semiconducting *t*-Se and opens new possibilities for future applications.

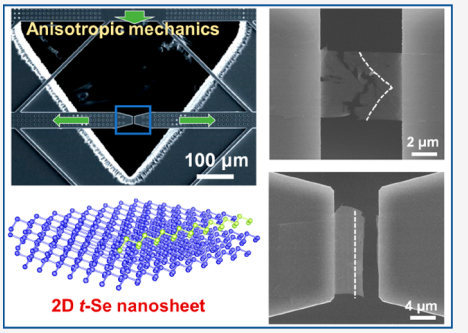

KEYWORDS: *2D t-Se nanosheets, anisotropic mechanical properties, in situ nanomechanical testing, MD simulation, DFT calculation*

INTRODUCTION

Trigonal selenium (*t*-Se) has recently emerged as a promising semiconductor material.[1−3] In particular, it can crystallize into an ultrathin 2D nanosheet (NS) assembled by parallel one-dimensional (1D) Se atomic chains (Figure 1a),[1] where the Se atoms are covalently bonded along the chain direction (*c*-axis) and the atomic chains are connected via van der Waals (vdW) interactions along the direction perpendicular to the chain axis (*a*/*b*-axis). This is in sharp contrast to typical 2D nanomaterials that usually possess layered structures, where the atoms are held together by covalent bonds within the layers with different chirality characteristics, and these layers are stacked together by relatively weak out-of-plane vdW force.[4,5] This unique 2D crystal structure not only enriches the 2D nanomaterials family but also endows it extraordinary multifunctional properties including nonlinear optical responses, high photoconductivity, piezoelectricity, thermoelectricity, etc.[1,6]

The anisotropy structures of materials generally play critical roles in their practical applications, and the 2D materials are no exceptions. For example, the in-plane anisotropic structure of 2D black phosphorus (BP) can lead to a variety of Raman responses reflecting thermal and electrical property variations along different directions, greatly expanding its applications.[7] Such structural anisotropy can be clearly demonstrated in ultrathin BPs by the remarkable differences among the Raman shift rates of A_g^1, B_{2g}, and A_g^2 modes along different strain directions, where the maximum Raman shift rate of B_{2g} mode can reach approximately -11 $cm^{-1}/\%$.[8] Although the in-plane mechanical properties of 2D materials have been intensively investigated using a series of advanced nanomechanical testing techniques, such as atomic force microscope (AFM) indentation and *in situ* scanning electron microscope (SEM)/transmission electron microscope (TEM) tension,[9−15] the reports on the mechanical anisotropy correlated to anisotropic structures are very limited. It is thus important to systematically study the mechanical anisotropy effects in 2D materials.

In this work, the structural anisotropy of 2D *t*-Se NSs under uniaxial tensile strain along the *c*-axis and *a*/*b*-axis was first studied using a simple bending apparatus combined with Raman spectroscopy. Additionally, tensile mechanical properties and fracture behaviors of 2D *t*-Se NSs along these two distinctive directions were studied using a quantitative *in situ* SEM nanomechanical testing platform combined with molecular dynamics (MD) simulations and density functional theory (DFT) calculations. This work could provide an in-depth understanding on the roles of structure-dependent mechanical anisotropy effects in 2D materials, paving the way for utilizing such effects in real applications.

Received: June 12, 2021
Revised: September 18, 2021

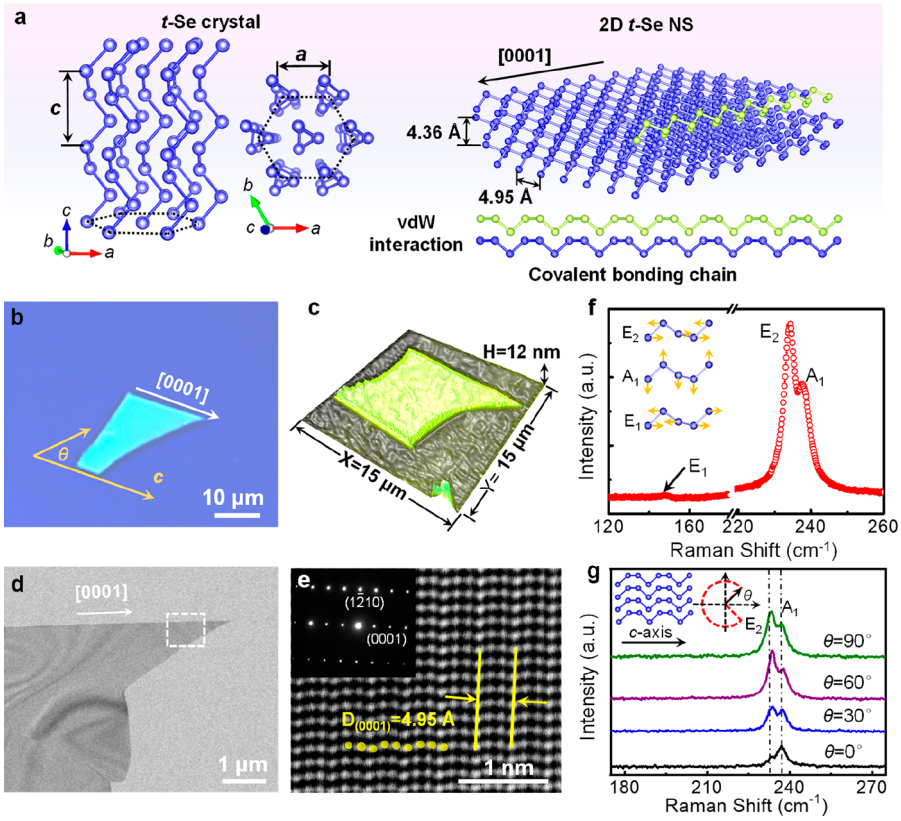

Figure 1. Characterization of 2D *t*-Se NSs. (a) Schematic for the lattice structure of *t*-Se crystal, where parallel Se atomic chains are packed together by vdW interaction. These atomic Se chains could arrange parallel into ultrathin NS in 2D form. (b) Optical microscopy image of a 12 nm thick *t*-Se NS and (c) corresponding AFM height profile. (d) Low-magnificent TEM image of *t*-Se NS. (e) HAADF-STEM image of *t*-Se NS, where the lattice spacing of 0.495 nm is assigned to (0001) faces, and the Se atomic chain is illustrated by yellow balls. The inset shows corresponding SAED pattern of the *t*-Se NS with zone axis along the *a* axis. (f) Raman spectra of *t*-Se NS, where the inset illustrates the corresponding lattice vibration pattern of E_2, A_1, and E_2 Raman modes, respectively. (g) Raman spectra of *t*-Se as a function of θ.

RESULTS AND DISCUSSION

The 2D *t*-Se was obtained using a simple physical vacuum deposition (PVD) method (Section S1, Figure S1).[3] The thin *t*-Se NS displays light-blue color with irregular trapezium shapes, and the lateral dimension could reach up to 30 μm with the smallest thickness of 12 nm (Figure 1b,c, Figure S2). High-angle annular dark-field scanning transmission electron microscopy (HAADF-STEM) was performed to investigate the crystalline orientation of *t*-Se NS (Figure 1d,e), where the helical Se atomic chains can be clearly identified and marked by the yellow balls in Figure 1e. The lattice spacing was measured to be 0.485 nm and can be assigned to (0001) planes, which is in excellent agreement with the theoretical calculations.[16] Combining the low-magnification TEM with selected area electron diffraction (SAED) pattern (inset in Figure 1e), we can determine that the *t*-Se NS tends to crystallize with straight edges in parallel with the [0001] direction.

We employed regular and polarized Raman spectroscopy to further explore the structural anisotropy of *t*-Se NSs. However, it is noted that the *t*-Se NS is very sensitive to the laser irradiation, and it could quickly degrade or become amorphous due to the low melting point of only 232 °C.[3] To resolve this issue and obtain reliable Raman signal, monolayer *h*-BN with high thermal conductivity was introduced to fabricate a novel *h*-BN/*t*-Se/*h*-BN sandwich structure (Section S2, Figure S3). The crystalline integrity of *t*-Se NS can thus be well preserved after Raman laser irradiation since heat can efficiently dissipate through *h*-BN layers. Figure 1f presents the typical Raman spectrum of *t*-Se NS in the range from 120 to 260 cm^{-1}, where three active Raman modes can be detected. The most intense peak located at 233 cm^{-1} belongs to the E_2 mode, which is caused by asymmetric stretching of atoms along *c*-axis. The A_1 mode at 237 cm^{-1} is introduced by the chain expansion where Se atoms moves along in-plane direction.[16] It should be noted that the E_1 mode located at 145 cm^{-1} is extremely difficult to be detected; thus we mainly focused on the A_1 and E_2 modes in the following discussion. Angle-resolved polarized Raman spectroscopy was also performed to identify the crystallographic orientation and anisotropic crystal structure of *t*-Se. As presented in Figure 1g, both E_2 and A_1 modes exhibit high dependence on θ. Here, θ is defined as the angle between the *c* axis of *t*-Se NS and the incident photon polarization. The extracted peak intensity of different vibration modes could be fitted with Lorentz function and plotted into polar figures. As shown in Figure S4, the fitted curves based on the calculations are in good agreement with the experimental data. The E_2 mode has four branches, with maxima and minima at 45° and 90°. The A_1 mode exhibits a two-lobed shape, with the maximum at an angle of ~90°, coinciding with the direction vertical to the straight edge of Se NS.[17] Thus, we can confirm that the 2D *t*-Se NS crystallizes with straight edge along the *c*-axis. The detailed explanation for the structural anisotropy by Raman signals is in Section S3.

https://doi.org/10.1021/acs.nanolett.1c02294
Nano Lett. XXXX, XXX, XXX−XXX

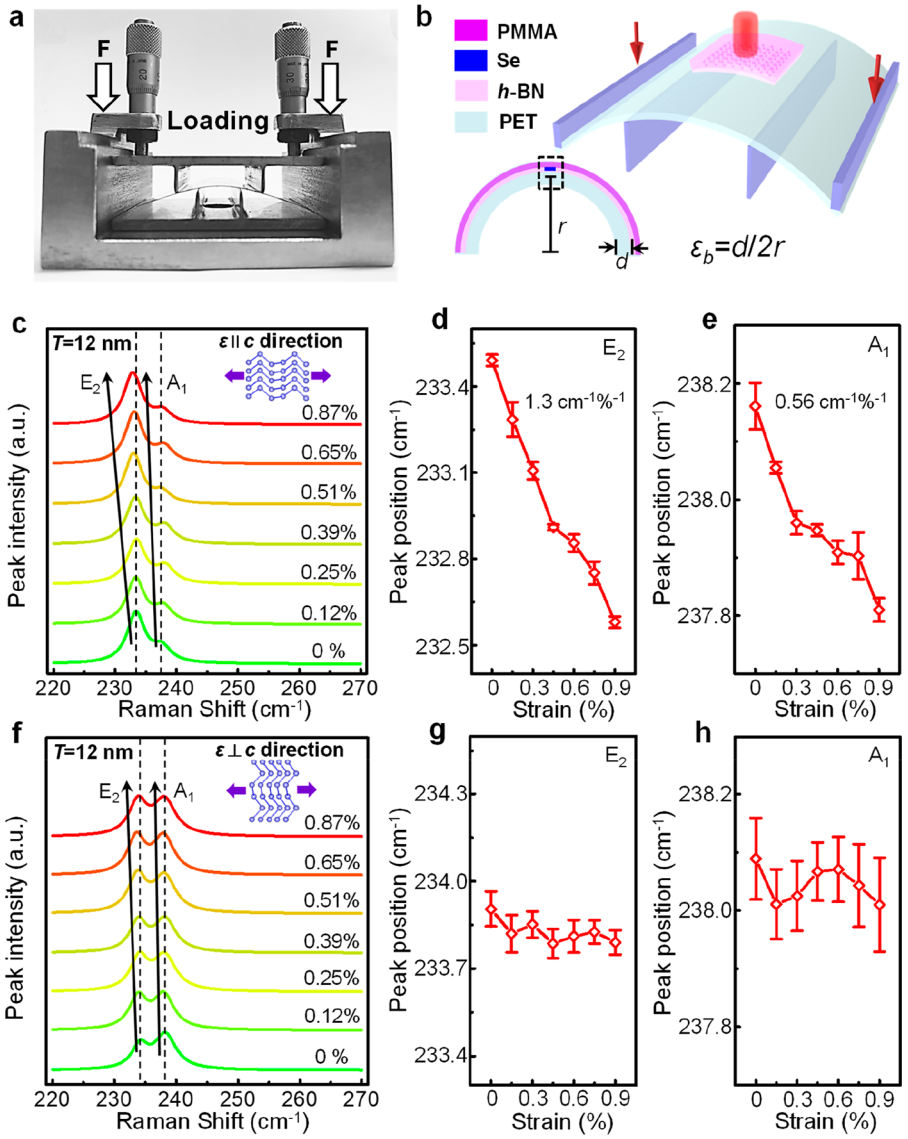

Figure 2. Anisotropic Raman response of *t*-Se NS under uniaxial strain along the *c*-axis and *a*/*b*-axis. (a) Photograph of the four-point bending system for Raman testing. This testing method is usually used to apply orthogonal in-plane strain along specific directions. (b) Schematic for the Raman testing setup. (c) Evolution of Raman spectra of the encapsulated *t*-Se NS on PET substrate under uniaxial strain ε along the *c*-axis. (d, e) Corresponding Raman shifts of E_2 and A_1 modes as a function of ε along the *c*-axis. (f) Evolution of Raman spectra under the uniaxial strain ε along *a*/*b*-axis. (g, h) Corresponding Raman shifts as a function of ε along the *a*/*b*-axis.

To reveal the anisotropic structural evolution of *t*-Se NSs under tensile deformation, we built a four-point bending instrument, with the samples on the top surface that is subjected to tension, to investigate the direction-dependent Raman response of *t*-Se NSs under uniaxial tensile strain (Figure 2a,b). This technique has been successfully applied to study the Raman response of various 2D materials under tensile strain.[8,18−20] In detail, by use of the PMMA-assisted wet transfer technique, monolayer *h*-BN film was first transferred on the 1 mm PET substrate. After the direct transfer of *t*-Se NSs by using a W probe under the optical microscope, another monolayer *h*-BN film is introduced using the same process, forming an *h*-BN/*t*-Se/*h*-BN sandwich structure. Finally, a thin layer (about 200 nm) of PMMA is spin-coated on PET surface to prevent the slippage and protect the ultrathin *t*-Se from degradation under ambient conditions. The clamping role of PMMA was confirmed by the observation that the position of Raman modes does not show any shift after 100 times of bending with tensile strain up to 0.84% (Figure S5). The bending strain ε_b can be estimated by $\varepsilon_b = d/(2r)$, where *d* and *r* represent the thickness and radius of curvature of the bent PET substrate, respectively (Figure 2b). As the thickness of the *t*-Se NS sample is much smaller than the thickness of PET, the induced strain to the flakes can be assumed to be the same as the applied strain to the PET substrate. It was noted that when $r \geq d$, the thin film sample on top of the PET substrate can be assumed to be under pure tensile loading. In this study, the Raman responses of strained *t*-Se NSs along two orthogonal directions (*c*-axis and *a*/*b*-axis) were investigated in the nonpolarized configuration. The detailed setup and testing process are in Section S4 and Figure S6.

As shown in Figure 2c, both E_2 and A_1 Raman modes exhibit a significant red-shift, which suggests that the associated restoring force in vibration modes of *t*-Se could be greatly weakened by tensile strain.[8,19] The shift rate can be calculated according to $\omega^* = \partial\omega/\partial\varepsilon$, where ω represents the Raman

https://doi.org/10.1021/acs.nanolett.1c02294
Nano Lett. XXXX, XXX, XXX−XXX

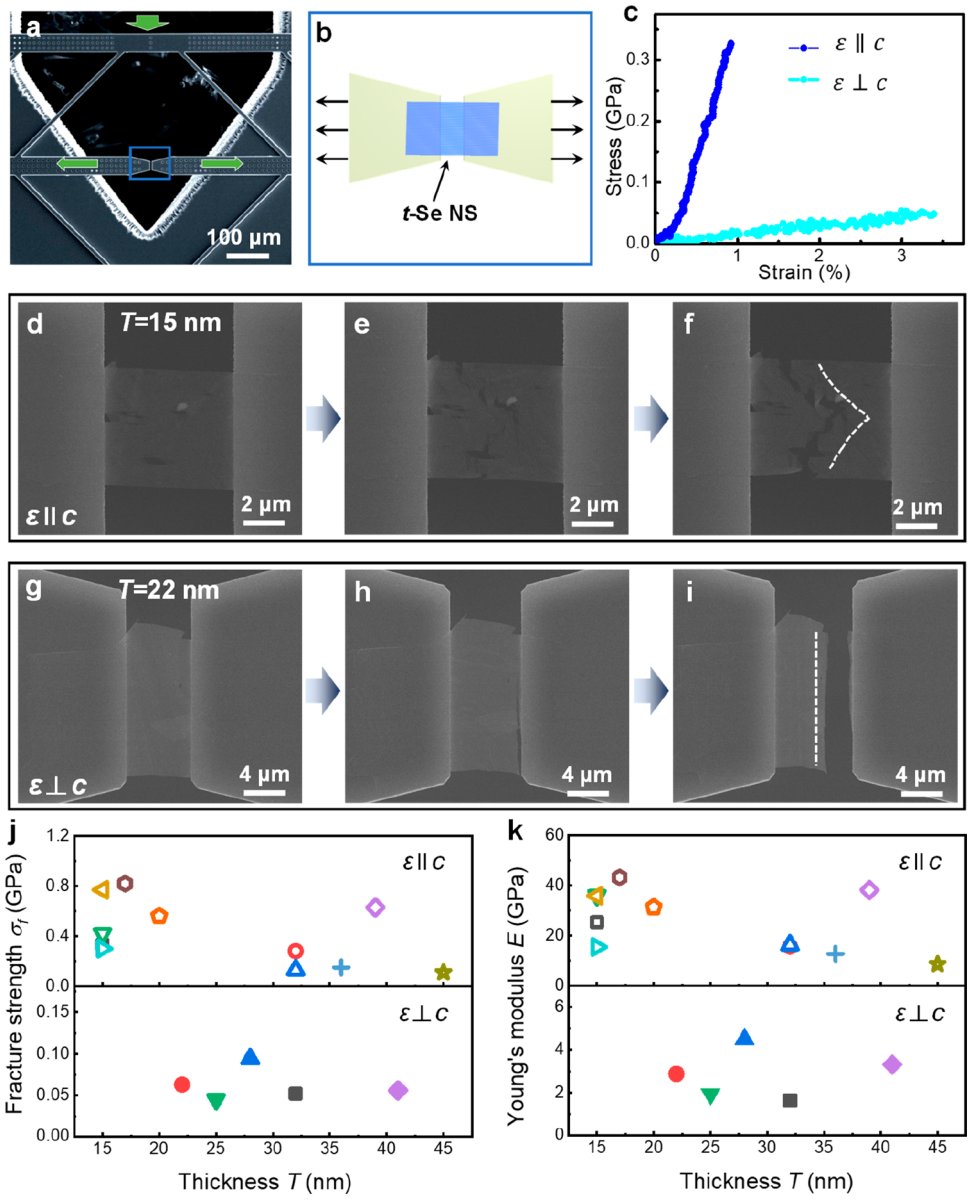

Figure 3. *In situ* tensile testing of 2D *t*-Se NS. (a) SEM image of the nanomechanical device. (b) Schematic for the tension of individual *t*-Se NSs, where the loading is applied along the *c*-axis and *a*/*b*-axis, respectively. (c) Tensile $\sigma-\varepsilon$ curves along two orthogonal directions. (d–f) Snapshots of *t*-Se NS (*c*-#1) before and after loading along *c*-axis. (g–i) Snapshots of *t*-Se NS (*a*/*b*-#3) before and after loading along the *a*/*b*-axis. (j, k) Fracture strength and Young's modulus of *t*-Se NSs along two orthogonal directions.

frequency. The ω^* of the E_2 mode could reach up to 1.3 cm^{-1} $\%^{-1}$ while ω^* of A_1 mode is only 0.56 cm^{-1} $\%^{-1}$, suggesting that these two vibration modes response differently (Figure 2d,e). The E_2 mode of *t*-Se represents the motion of Se atoms along *c*-axis, while the A_1 mode reflects the radical expansion of Se atom chains along in-plane direction (Figure 1f). The length of Se–Se covalent bonds was obviously elongated under tensile strain, resulting in the decrease of atomic interaction and reduction of vibration frequency.[21] However, the tensile strain along the *c*-axis could only slightly decrease the equilateral triangle projection of 1D Se atomic chains, leading to the relatively small red shift of the A_1 mode. In contrast, the response of Raman modes in *t*-Se NS shows remarkable difference when the tensile strain is applied along the *a*/*b*-axis. As shown in Figure 2f–h, the peak positions of E_2 and A_1 modes only fluctuate with no obvious change even as applied strain reaches up to 0.86%. As mentioned before, interaction between Se atoms has distinct anisotropy in the *t*-Se crystal, i.e., covalent bonding along the *c*-axis and vdW interaction along the *a*/*b*-axis. Therefore, the strain along the *a*/*b*-axis cannot be effectively transferred to the individual Se helical chain due to the weak vdW interaction, leading to the extremely weak strain sensitivity of Raman modes in this configuration. In this study, similar behaviors were also revealed in some samples with applied compression strains (Section S4, Figure S7). This pronounced anisotropy of Raman responses in strained *t*-Se NS further demonstrated its anisotropic structures.

Next, we employed an *in situ* SEM nanomechanical testing system enabled by a nanoindenter to quantitatively study the perceived anisotropic mechanical properties of *t*-Se NSs (Figure 3a,b).[14,15,22−24] The ribbon-like *t*-Se NS was first cut to several micrometer long strips and then transferred onto the sample shuttles using a sharp W probe under the optical

https://doi.org/10.1021/acs.nanolett.1c02294
Nano Lett. XXXX, XXX, XXX−XXX

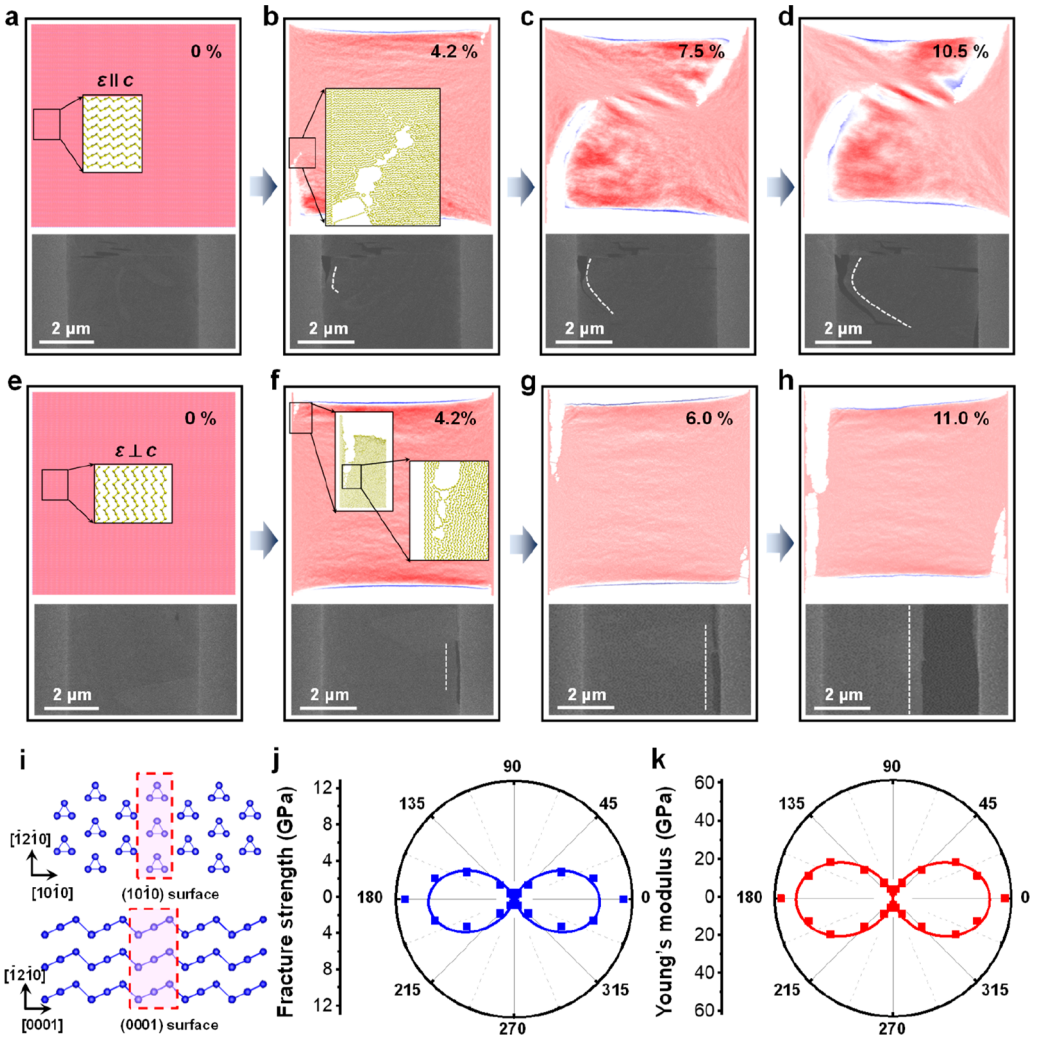

Figure 4. Theoretical calculations on the anisotropic fracture behaviors of 2D *t*-Se NS. (a–h) MD simulation snapshots with different tensile strains (upper) along two orthogonal directions, where atoms in MD snapshots are colored according to the height in the out-of-plane direction, as well as the corresponding SEM images of *t*-Se NSs showing similar fracture modes (lower). (i) Atomic structure of *t*-Se slabs after DFT relaxation for calculating surface energy. (j, k) Angle dependence of normalized fracture strength and Young's modulus obtained by DFT simulation.

microscope. The testing device loaded with samples was actuated by the in-SEM nanoindenter, and uniaxial tension forces can be applied to individual *t*-Se NS samples through a push–pull mechanism. The edge of strips along *c*-axis is very smooth and flat, which could serve as a natural guideline and allows us to determine and align two orthogonal crystalline orientations with the loading direction. Furthermore, the crystalline orientations of all samples were accurately identified using angle-dependent Raman spectroscopy before sample transfer. The detailed testing procedures can be found in Section S5.

Figure 3c shows typical tensile stress versus strain curves of *t*-Se NSs along *c*-axis and *a*/*b*-axis (*c*-#1 and *a*/*b*-#3 as numbered in Table S1). Figure 3d–i shows the corresponding snapshots of the tensile fracture experiments along these two directions, respectively (see corresponding tensile Movie S1 and Movie S2 in Supporting Information). As evidenced by the linear stress–strain curves, the stress increases to a maximum value before rapidly dropping to zero, indicating a typical brittle fracture behavior. The mechanical anisotropy effects are quite obvious. From Table S1, it can be clearly seen that the measured fracture strength σ_f and Young's modulus E along the *c*-axis (0.11–0.82 GPa and 8.59–43.24 GPa, respectively) are much higher than those along the *a*/*b*-axis (0.045–0.094 GPa and 1.63–4.50 GPa, respectively). These big differences are attributed to the bonding nature along the two directions, i.e., strong covalent bonding along the *c*-axis vs weak vdW interactions along the *a*/*b*-axis. In addition, we found that the σ_f and E along the *c*-axis appears to decrease with increasing thicknesses, similar to typical size-effect. However, they are less dependent on thicknesses along the *a*/*b*-axis. More interestingly, it was observed that the crack propagation of *t*-Se NS sample follows a typical "zig-zg" path under the tensile loading along the *c*-axis (Figure 3f) while the crack front is flat when the loading was along the *a*/*b*-axis (Figure 3i). In this study, in order to further understand the fracture process and corresponding crystalline orientation of *t*-Se NSs, the local regions of fracture surfaces of tested samples were examined by HRTEM combining with the SAED pattern, as shown in Figure S8. These anisotropic mechanical behaviors are quite different from some other 2D materials such as black phosphorus,[25,26] where the in-plane mechanical anisotropy is not significant and is mainly caused by the anisotropy of the covalently bonded honeycomb-like nanostructures. It should

https://doi.org/10.1021/acs.nanolett.1c02294
Nano Lett. XXXX, XXX, XXX–XXX

be mentioned that this experiment also provides a rare opportunity to quantitatively estimate the vdW interaction strength in 2D single crystals, which is comparable with that in well-known carbon nanotube-based nanomaterial systems.[27,28]

To better understand the anisotropic fracture behaviors from the atomic viewpoint, classic MD simulation was performed. A molecular model of 170 nm × 170 nm *t*-Se NS with thickness ∼0.6 nm (one layer of atom chain) was established, and a uniform tensile loading was applied along two orthogonal directions (see detailed simulation process in Section S6). The tensile snapshots are shown in Figure 4a−h (see corresponding tensile Movie S3 and Movie S4 in Supporting Information). It was found that the tensile stress increases linearly with increase of strain along the *c*-axis. In the early stage, ε is mainly attributed to the stretching of the Se atomic chains. When ε increases to ∼3.7%, a tiny crack can be observed at the edge of *t*-Se NS, with the breakage of several Se atomic chains. With further increase of ε (up to the maximum 10.5%), more Se atomic chains were broken irregularly near the crack tip, and the fast release of elastic strain energy led to a "zigzg" fracture morphology (Figure 4d). It was observed that the zigzg crack propagation strongly correlates to the out-of-plane wavy deformation of the *t*-Se NS, which agrees with what was observed for the fracture of polycrystalline graphene.[29] The zigzag crack propagation effectively increases the crack growth resistance with more energy dissipation during facture process, as it has been observed in composites made of different material phases[30] or materials with defect tolerance.[31] This is widely observed in biomaterials but rarely seen in 2D materials, as they are usually brittle and can be easily fractured from a crack. This kind of fracture mode is in good agreement with earlier *in situ* SEM observations. On the other hand, σ also increases linearly with ε as the loading is applied along the *a*/*b*-axis, and an initial crack would appear when ε reaches up to a critical value (∼4%). Due to the relatively weak vdW interaction, individual Se atomic chains can be easily teared apart. Thus, the crack would catastrophically propagate along the chain direction, leading to the straight fracture edge (Figure 4h).

Additionally, we performed the DFT calculation to further reveal the mechanical anisotropy of *t*-Se NSs (see detailed calculation process in Section S7). On the basis of fracture mechanics theories, the surface energy γ on $(10\bar{1}0)$ and (0001) surfaces can be used to describe the material capability to resist fracture. As shown in Figure 4i, the surface energy can be defined as the excess energy of a slab relative to the perfect nanosheet divided by the nominal area of two free surfaces of the slab.[15] The surface energy on surfaces perpendicular to the *c*-axis and the *a*/*b*-axis was calculated to be 3.88 eV/nm^2 and 0.20 eV/nm^2, respectively, which confirms that the fracture resistance of covalently bonded Se atomic chains is much stronger than that of Se atomic chain bundles connected by vdW interaction. The DFT calculated σ_f and *E* of *t*-Se NSs along different loading directions (0−90°) were investigated and presented in Figure 4j,k, where angles θ = 0° and θ = 90° refer to the loading directions along the *c*-axis and *a*/*b*-axis, respectively. It was found that that σ_f and *E* are highly dependent on θ. With increase of θ, σ_f and *E* nonlinearly increase until reaching maximum values when stretching and breaking the covalent bonds in Se atomic chains. It is worth noting that the measured σ_f and *E* are much lower than the theoretical prediction with relatively large variation, which can be attributed to the procedure-induced flaws/cracks in the *t*-Se NSs.

CONCLUSIONS

In summary, the structural and mechanical anisotropy of a novel asymmetrical 2D *t*-Se NS was experimentally and theoretically investigated. It was found that there was a strong Raman peak shift under tensile strain along the *c*-axis due to the stretching of covalent Se atomic chains. However, the Raman peak shift is much less sensitive to the tensile strain along the orthogonal direction because of the weak vdW interaction between Se atomic chains. The *in situ* nanomechanical SEM testing shows that Young's modulus and the fracture strength along the *c*-axis are much higher than that along *a*/*b*-axis. In addition, the "zigzg" and "straight" fracture modes were observed along these two directions. MD simulations revealed that the "zigzg" fracture morphology is mainly attributed to the irregular breakage of Se atomic chains near the crack tip, and the "straight" fracture morphology is resulting from stable interface crack between Se atomic chains. Finally, DFT calculations revealed that the mechanical anisotropy of *t*-Se could also track back to the differences in surface energy in these two orthogonal orientations. Our work sheds light into the intrinsic structural and mechanical anisotropic properties of 2D *t*-Se crystals, laying the foundation for promising applications of advanced 2D materials.

ASSOCIATED CONTENT

Supporting Information

The Supporting Information is available free of charge at https://pubs.acs.org/doi/10.1021/acs.nanolett.1c02294.

More details for preparation of materials; sample preparation for Raman testing; setup of Raman characterization for anisotropic structure of 2D *t*-Se NSs; Raman testing under tensile and compressive strains; *in situ* tensile testing process; MD simulation and DFT calculation (PDF)

Tensile Movie S1 (MP4)

Tensile Movie S2 (MP4)

Tensile Movie S3 (MP4)

Tensile Movie S4 (MP4)

AUTHOR INFORMATION

Corresponding Authors

Chao Wang − *Center for Composite Materials and Structures, Harbin Institute of Technology, Harbin 150080, China; Department of Materials Science and NanoEngineering, Rice University, Houston, Texas 77005, United States;* orcid.org/0000-0002-1816-5749; Email: chaowang@hit.edu.cn

Xiaodong He − *Center for Composite Materials and Structures, Harbin Institute of Technology, Harbin 150080, China; Shenzhen STRONG Advanced Materials Research Institute Co., Ltd., Shenzhen 518000, P. R. China;* Email: hexd@hit.edu.cn

Peide D. Ye − *School of Electrical and Computer Engineering, Purdue University, West Lafayette, Indiana 47907, United States;* orcid.org/0000-0001-8466-9745; Email: yep@purdue.edu

Jun Lou − *Department of Materials Science and NanoEngineering, Rice University, Houston, Texas 77005,*

https://doi.org/10.1021/acs.nanolett.1c02294
Nano Lett. XXXX, XXX, XXX−XXX

United States; orcid.org/0000-0002-4351-9561; Email: jlou@rice.edu

Authors

Jing-Kai Qin − *Center for Composite Materials and Structures, Harbin Institute of Technology, Harbin 150080, China; Sauvage Laboratory for Smart Materials, School of Materials Science and Engineering, Harbin Institute of Technology (Shenzhen), Shenzhen 518055, China; School of Electrical and Computer Engineering, Purdue University, West Lafayette, Indiana 47907, United States;* orcid.org/0000-0002-0737-3614

Chao Sui − *Center for Composite Materials and Structures, Harbin Institute of Technology, Harbin 150080, China; Department of Materials Science and NanoEngineering, Rice University, Houston, Texas 77005, United States*

Zhao Qin − *Department of Civil and Environmental Engineering, Syracuse University, Syracuse, New York 13244, United States;* orcid.org/0000-0001-5696-8553

Jianyang Wu − *Department of Physics, Research Institute for Biomimetics and Soft Matter, Fujian Provincial Key Laboratory for Soft Functional Materials Research, Xiamen University, Xiamen 361005, China;* orcid.org/0000-0002-9094-4835

Hua Guo − *Department of Materials Science and NanoEngineering, Rice University, Houston, Texas 77005, United States*

Liang Zhen − *Sauvage Laboratory for Smart Materials, School of Materials Science and Engineering, Harbin Institute of Technology (Shenzhen), Shenzhen 518055, China;* orcid.org/0000-0001-6159-8972

Cheng-Yan Xu − *Sauvage Laboratory for Smart Materials, School of Materials Science and Engineering, Harbin Institute of Technology (Shenzhen), Shenzhen 518055, China;* orcid.org/0000-0002-7835-6635

Yang Chai − *Department of Applied Physics, The Hong Kong Polytechnic University, Hong Kong, China;* orcid.org/0000-0002-8943-0861

Complete contact information is available at: https://pubs.acs.org/10.1021/acs.nanolett.1c02294

Author Contributions

[∞]J.-K.Q. and C.S. contributed equally. J.K.Q. prepared the *t*-Se NS and performed the Raman testing. C.S., H.G., and C.W. performed the *in situ* mechanical testing. Z.Q. and J.W. supervised and performed the MD and DFT calculations. L.Z., C.-Y.X., Y.C., and P.D.Y. supervised the design of the bending system and Raman testing. X.H. and J.L. supervised the mechanical testing. X.H., C.W., P.D.Y., and J.L. conceived the idea. J.-K.Q., C.S., C.W., and J.L. co-wrote the manuscript.

Notes

The authors declare no competing financial interest.

■ ACKNOWLEDGMENTS

The authors gratefully acknowledge the financial support by the National Natural Science Foundation of China (NSFC, Grant No. 11872164) and Natural Science Foundation of Guangdong Province (Grant No. 2021A1515012423). This work was also supported by Shenzhen Science and Technology Program (Grant No. KQTD20161128143030555) and Research Grant Council of Hong Kong (15205318). H. G and J. L acknowledge the support by the Welch Foundation grant C-1716. C. W. thanks the support of China Scholarship Council for overseas study (Grant No. 201606125054).

■ REFERENCES

(1) Qin, J. K.; Qiu, G.; Jian, J.; Zhou, H.; Yang, L. M.; Charnas, A.; Zemlyanov, D. Y.; Xu, C. Y.; Xu, X. F.; Wu, W. Z.; Wang, H. Y.; Ye, P. D. D. Controlled Growth of a Large-Size 2D Selenium Nanosheet and Its Electronic and optoelectronic Applications. *ACS Nano* **2017**, *11* (10), 10222−10229.

(2) Andharia, E.; Kaloni, T. P.; Salamo, G. J.; Yu, S. Q.; Churchill, H.; Barraza-Lopez, S. Exfoliation energy, quasiparticle band structure, and excitonic properties of selenium and tellurium atomic chains. *Phys. Rev. B: Condens. Matter Mater. Phys.* **2018**, *98* (3), 035420.

(3) Qin, J. K.; Zhou, F. C.; Wang, J. L.; Chen, J. W.; Wang, C.; Guo, X. Y.; Zhao, S. X.; Pei, Y.; Zhen, L.; Ye, P. D. D.; Lau, S. P.; Zhu, Y.; Xu, C. Y.; Chai, Y. Anisotropic Signal Processing with Trigonal Selenium Nanosheet Synaptic Transistors. *ACS Nano* **2020**, *14* (8), 10018−10026.

(4) Liu, Y.; Huang, Y.; Duan, X. F. Van der Waals Integration before and beyond Two-dimensional Materials. *Nature* **2019**, *567* (7748), 323−333.

(5) Kufer, D.; Konstantatos, G. Highly Sensitive, Encapsulated MoS_2 Photodetector with Gate Controllable Gain and Speed. *Nano Lett.* **2015**, *15*, 7307−7313.

(6) Luo, L. B.; Yang, X. B.; Liang, F. X.; Jie, J. S.; Li, Q.; Zhu, Z. F.; Wu, C. Y.; Yu, Y. Q.; Wang, L. Transparent and flexible selenium nanobelt-based visible light photodetector. *CrystEngComm* **2012**, *14*, 1942−1947.

(7) Luo, Z.; Maassen, J.; Deng, Y.; Du, Y.; Garrelts, R. P.; Lundstrom, M. S.; Ye, P. D.; Xu, X. Anisotropic in-plane thermal conductivity observed in few-layer black phosphorus. *Nat. Commun.* **2015**, *6*, 8572.

(8) Li, Y.; Hu, Z.; Lin, S.; Lai, S. K.; Ji, W.; Lau, S. P. Giant Anisotropic Raman Response of Encapsulated Ultrathin Black Phosphorus by Uniaxial Strain. *Adv. Funct. Mater.* **2017**, *27*, 1600986.

(9) Lee, C.; Wei, X.; Kysar, J. W.; Hone, J. Measurement of the Elastic Properties and Intrinsic Strength of Monolayer Graphene. *Science* **2008**, *321* (5887), 385−388.

(10) Cao, C.; Mukherjee, S.; Howe, J. Y.; Perovic, D. D.; Sun, Y.; Singh, C. V.; Filleter, T. Nonlinear fracture toughness measurement and crack propagation resistance of functionalized graphene multilayers. *Science Advances* **2018**, *4* (4), eaao7202.

(11) Lipatov, A.; Lu, H. D.; Alhabeb, M.; Anasori, B.; Gruverman, A.; Gogotsi, Y.; Sinitskii, A. Elastic properties of 2D Ti3C2Tx MXene monolayers and bilayers. *Sci. Adv.* **2018**, *4* (6), eaat0491.

(12) Cao, G.; Gao, H. Mechanical properties characterization of two-dimensional materials via nanoindentation experiments. *Prog. Mater. Sci.* **2019**, *103*, 558−595.

(13) Lee, G. H.; Cooper, R. C.; An, S. J.; Lee, S.; van der Zande, A.; Petrone, N.; Hammerberg, A. G.; Lee, C.; Crawford, B.; Oliver, W.; Kysar, J. W.; Hone, J. High-Strength Chemical-Vapor-Deposited Graphene and Grain Boundaries. *Science* **2013**, *340*, 1073−1076.

(14) Zhang, P.; Ma, L.; Fan, F.; Zeng, Z.; Peng, C.; Loya, P. E.; Liu, Z.; Gong, Y.; Zhang, J.; Zhang, X.; Ajayan, P. M.; Zhu, T.; Lou, J. Fracture toughness of graphene. *Nat. Commun.* **2014**, *5*, 3782.

(15) Yang, Y.; Li, X.; Wen, M.; Hacopian, E.; Chen, W.; Gong, Y.; Zhang, J.; Li, B.; Zhou, W.; Ajayan, P. M.; Chen, Q.; Zhu, T.; Lou, J. Brittle Fracture of 2D $MoSe_2$. *Adv. Mater.* **2017**, *29* (2), 1604201.

(16) Martin, R. M.; Lucovsky, G.; Helliwell, K. Intermolecular bonding and lattice dynamics of Se and Te. *Phys. Rev. B* **1976**, *13* (4), 1383−1395.

(17) Qiu, G.; Du, Y.; Charnas, A.; Zhou, H.; Jin, S.; Luo, Z.; Zemlyanov, D. Y.; Xu, X.; Cheng, G. J.; Ye, P. D. Observation of Optical and Electrical In-Plane Anisotropy in High-Mobility Few-Layer $ZrTe_5$. *Nano Lett.* **2016**, *16*, 7364−7369.

(18) Wang, Y.; Cong, C.; Fei, R.; Wang, W.; Chen, Y.; Cao, B.; Yang, L.; Yu, T. Remarkable anisotropic phonon response in uniaxially strained few-layer black phosphorus. *Nano Res.* **2015**, *8*, 3944−3953.

(19) Du, Y.; Qiu, G.; Wang, Y.; Si, M.; Xu, X.; Wu, W.; Ye, P. D. One-Dimensional van der Waals Material Tellurium: Raman Spectroscopy under Strain and Magneto-Transport. *Nano Lett.* **2017**, *17*, 3965−3973.
(20) Lin, P.; Zhu, L.; Li, D.; Xu, L.; Pan, C.; Wang, Z. Piezo-Phototronic Effect for Enhanced Flexible MoS_2/WSe_2 van der Waals Photodiodes. *Adv. Funct. Mater.* **2018**, *28*, 1802849.
(21) Du, Y.; Maassen, J.; Wu, W.; Luo, Z.; Xu, X.; Ye, P. D. Auxetic Black Phosphorus: A 2D Material with Negative Poisson's Ratio. *Nano Lett.* **2016**, *16* (10), 6701−6708.
(22) Ganesan, Y.; Peng, C.; Lu, Y.; Loya, P.; Moloney, P.; Barrera, E.; Yakobson, B.; Tour, J. M.; Ballarini, R.; Lou, J. Interface Toughness of Carbon Nanotube Reinforced Epoxy Composites. *ACS Appl. Mater. Interfaces* **2011**, *3* (2), 129−134.
(23) Hacopian, E. F.; Yang, Y.; Ni, B.; Li, Y.; Li, X.; Chen, Q.; Guo, H.; Tour, J. M.; Gao, H.; Lou, J. Toughening Graphene by Integrating Carbon Nanotubes. *ACS Nano* **2018**, *12*, 7901−7910.
(24) Fang, Q.; Sui, C.; Wang, C.; Zhai, T.; Zhang, J.; Liang, J.; Guo, H.; Sandoz-Rosado, E.; Lou, J. Strong and flaw-insensitive two-dimensional covalent organic frameworks. *Matter* **2021**, *4*, 1017−1028.
(25) Tao, J.; Shen, W.; Wu, S.; Liu, L.; Feng, Z.; Wang, C.; Hu, C.; Yao, P.; Zhang, H.; Pang, W.; Duan, X.; Liu, J.; Zhou, C.; Zhang, D. Mechanical and Electrical Anisotropy of Few-Layer Black Phosphorus. *ACS Nano* **2015**, *9* (11), 11362−11370.
(26) Fei, R.; Yang, L. Strain-engineering the anisotropic electrical conductance of few-layer black phosphorus. *Nano Lett.* **2014**, *14* (5), 2884−2889.
(27) Qu, L.; Dai, L.; Stone, M.; Xia, Z.; Wang, Z. Carbon nanotube arrays with strong shear binding-on and easy normal lifting-off. *Science* **2008**, *322*, 238−242.
(28) Sui, C.; Luo, Q.; He, X.; Tong, L.; Zhang, K.; Zhang, Y.; Zhang, Y.; Wu, J.; Wang, C. A study of mechanical peeling behavior in a junction assembled by two individual carbon nanotubes. *Carbon* **2016**, *107*, 651−657.
(29) Jung, G.; Qin, Z.; Buehler, M. J. Molecular mechanics of polycrystalline graphene with enhanced fracture toughness. *Extreme Mech. Lett.* **2015**, *2*, 52−59.
(30) Libonati, F.; Gu, G. X.; Qin, Z.; Vergani, L.; Buehler, M. J. Bone-Inspired Materials by Design: Toughness Amplification Observed Using 3D Printing and Testing. *Adv. Eng. Mater.* **2016**, *18*, 1354−1363.
(31) Wu, J.; Qin, Z.; Qu, L.; Zhang, H.; Deng, F.; Guo, M. Natural hydrogel in American lobster: a soft armor with high toughness and strength. *Acta Biomater.* **2019**, *88*, 102−110.

https://doi.org/10.1021/acs.nanolett.1c02294
Nano Lett. XXXX, XXX, XXX−XXX